MDPI

Article

The Effect of La on the Surface Properties of Plasma Nitrided CoCrCuFeNi High-Entropy Alloys at 440 Degrees Celsius

Yifan Wang [1], Yuan You [1,*], Mufu Yan [2], Yanxiang Zhang [2], Wenping Sheng [1], Yan Wang [1], Shimiao Xu [1], Feng Gu [1], Chaohui Wang [1] and Weidong Cheng [1]

[1] Heilongjiang Provincial Key Laboratory of Polymeric Composition Materials, School of Materials Science and Engineering, Qiqihar University, Qiqihar 161006, China; blue12black@163.com (W.S.); 19917729878@163.com (Y.W.)

[2] National Key Laboratory for Precision Hot Processing of Metals, School of Materials Science and Engineering, Harbin Institute of Technology, Harbin 150001, China

* Correspondence: greatyouyuan@163.com

Abstract: This paper investigates the effect of the element La on plasma nitriding of the CoCrCuFeNi high-entropy alloy (HEA) at 440 °C for 8, 16, and 24 h. The phase composition, morphology, and hardness distribution of the nitrided layer are characterized using XRD, optical microscopy, and a microhardness tester. Furthermore, the corrosion resistance is tested using an electrochemical workstation. The study evaluated the friction and wear performance using a testing machine and scanning electron microscope. The thickness of the effective hardening layer after 16 h of treatment with La was similar to that after 24 h of treatment without La. The addition of La significantly increased the growth rate constant of the effective hardening layer from 0.53×10^{-14} m^2/s to 0.72×10^{-14} m^2/s. In addition, an expanded FCC phase with greater interplanar spacing can be formed on the surface of the sample by introducing La into the plasma nitriding process. This indicates that the expanded FCC phase, with a higher concentration of interstitial nitrogen atoms, can effectively improve the corrosion resistance of the specimen surface. The corrosion rate of the specimen surface was reduced by 27.5% and the wear rate was reduced by 41.7% after 16 h of treatment with the addition of La compared to 24 h of nitriding without the addition of La. It has been shown that the addition of La to the plasma nitriding process results in a higher quality nitrided layer in a shorter time and also demonstrates that La has the potential to optimize the surface properties of plasma nitrided HEAs.

Keywords: high-entropy alloy; plasma nitriding; rare earth; kinetic; wear

1. Introduction

High-entropy alloys (HEAs), as a novel class of metallic materials, diverge fundamentally from traditional alloy systems in their design concept [1–3]. In conventional alloys, typically, one metal element serves as the matrix, supplemented by a small amount of other elements (Co, Cr, Ni, Al, etc.) to adjust the microstructure and enhance mechanical properties [4]. In contrast, high-entropy alloys consist of five or more principal elements, with each element's molar fraction ranging between 5% and 35% [5,6], collectively forming simple solid solution phases. This unique compositional strategy endows high-entropy alloys with numerous superior physical and chemical properties, such as high hardness, excellent wear resistance [7,8], outstanding fatigue resistance [9,10], strength retention at high temperatures [11–13], and thermal stability [14,15].

In specific application scenarios, researchers have employed traditional surface treatment technologies, including gas nitriding, to improve the surface performance of high-entropy alloys. However, studies on gas nitriding are relatively scarce. For instance, Meng et al. [16] treated an $Fe_{28.2}Ni_{18.8}Mn_{32.9}Al_{14.1}Cr_6$ high-entropy alloy with pure nitrogen gas nitriding at 1000 °C and 800 °C for 100 h. This treatment formed an aluminum-rich nitrided

zone on the sample surface, where the hardness significantly increased to 344 ± 18 HV (1000 °C) and 364 ± 8 HV (800 °C). After annealing at 1000 °C for 100 h, the maximum thickness of the nitrided zone could reach 1000 μm. Moreover, this research indicates that the performance enhancement after gas nitriding may be closely related to the spacing between the nitrided zones.

Meanwhile, plasma nitriding, as a surface modification technique, has been more widely applied in high-entropy alloys. Since 2009, scholars have begun to conduct plasma nitriding experiments on high-entropy alloys to enhance the performance of the material's surface layer and expand its application fields. Previous studies have focused on nitriding temperatures ranging from 490 °C [17] to 550 °C, using NH_3 or $N_2 + H_2$ as the nitriding atmospheres, with nitriding times between 9 and 45 h. After nitriding treatment, the maximum thickness of the modified layer could reach 92.2 μm [18], with a significant increase in hardness and the formation of a uniform nitrided layer. The nitrided layer on the high-entropy alloy improved wear resistance by 49 to 80 times [18] compared to its untreated high-entropy alloy counterpart. On the other hand, when comparing the nitrided high-entropy alloy to nitrided traditional steel, the high-entropy alloy demonstrated a 25 to 54 times [19] increase in wear resistance over the nitrided traditional steel material.

Tang et al. [20] conducted a study on the nitriding of high-entropy alloys. They found that the presence of aluminum (Al) significantly impacts nitrogen diffusion within the sample. The study indicates that the absence of aluminum results in the most effective nitrogen diffusion depth, leading to a nitrided layer that can reach a thickness of up to 33 μm. On the other hand, an increase in aluminum content reduces the thickness of the nitrided layer. Precisely, at an aluminum content of 0.5, the wear rate after nitriding is measured at 3.69×10^{-5} mm^3/N·m; an improvement compared to the untreated specimen wear rate of 6.38×10^{-4} mm^3/N·m. Although the study demonstrates that a nitrided layer of up to 33 μm enhances wear resistance, the 45 h nitriding duration may be excessively long from an industrial efficiency perspective.

Based on current research [18–23], plasma nitriding technology is an effective method for modifying surface properties. However, the efficiency of plasma nitriding is hindered by the sluggish diffusion effective in complex alloy matrices. To overcome the limitation of sluggish diffusion, previous studies have attempted to accelerate the nitriding process by adjusting process parameters, such as temperature and time, but these attempts have yet to resolve the diffusion bottleneck fully. Therefore, this study aims to explore a new method to improve nitriding efficiency.

Scholars have confirmed that rare earth elements can accelerate the nitriding process significantly. Research by Peng et al. [24] demonstrated that rare earth elements acted as catalysts in the plasma nitriding of 38CrMoAl steel, increasing the thickness of the modified layer and significantly enhancing the wear resistance of the co-nitrided layer. Bell et al. [25], in their review, elaborated on the role of rare earth elements in surface engineering, proposing mechanisms of rare earth chemical heat treatment, including promoting the generation of active atoms (such as carbon and nitrogen), accelerating the mass transfer process of active atoms, and the microalloying effect. Additionally, rare earth elements in the thermal spraying process of nickel-based coatings not only refine the microstructure of the coating and enhance the bonding strength between the coating and the substrate but also improve wear resistance and load-bearing capacity while purifying the interface. You et al. [26] have found, through first-principles calculations, that the element lanthanum (La) interacts with nitrogen atoms near the surface of the specimen, accelerating the movement of nitrogen atoms toward the specimen. Additionally, La atoms create reverse trapping zones within the specimen, facilitating the inward diffusion of nitrogen atoms. Furthermore, other research has experimentally shown that the element La can expedite the diffusion of nitrogen atoms in plasma nitriding [27,28].

Therefore, this study proposes introducing rare earth elements (lanthanum) to accelerate nitrogen diffusion during plasma nitriding of CoCrCuFeNi high-entropy alloys. The innovation of this method lies in the untapped potential of La in the surface modification of

high-entropy alloys. The integration of La aims to decrease the activation energy required for nitrogen diffusion. This results in an acceleration of the nitriding kinetic process and the production of thicker nitrided layer with improved surface properties without requiring higher temperatures or a longer treatment time.

2. Materials and Methods

High-entropy alloy ingots with a nominal composition of CoCrCuFeNi (at. %) (chemical composition listed in Table 1) were prepared by arc-melting. The ingots were remelted two times under a vacuum environment to ensure chemical homogeneity. The specimens were cut to 10 mm × 10 mm × 2 mm and then mechanically polished to 2000 grade with silicon carbide paper. The polished specimens were ultrasonically cleaned in alcohol before subsequent processing.

Table 1. Chemical compositions of as-cast CoCrCuFeNi HEA (at.%).

Composition	Co	Cr	Cu	Fe	Ni
Nominally	20	20	20	20	20
Actual	18.88	21.75	18.82	20.93	19.62

The plasma nitriding treatment was performed using a LDMC-30AFZ plasma nitriding furnace (Wuhan Shoufa Surface Engineering Co., Ltd., Wuhan, China) after the chamber was pumped to below 10 Pa by a rotary pump. The rare earth (RE) element used in the experiments was obtained from La (lanthanium) blocks with a volume of $(0.5 \times 0.5 \times 1)$ cm^3. The samples were uniformly tied to the sample holder with wire, and the La block was placed at the center of the sample holder. Nitriding experiments were performed in ammonia (NH$_3$) at 440 °C with flow rate of 100 mL/min, a gas pressure of 260 Pa during nitriding, and nitriding times of 8, 16, and 24 h (specific processes are listed in Table 2). Following plasma nitriding, the specimens were slowly cooled in a vacuum furnace. For comparative studies, plasma nitriding without La was also performed.

Table 2. Details of plasma nitriding of CoCrCuFeNi.

Identified Name	Temperature, °C	Time, h	Atmosphere	Gas Pressure, Pa
PN440-8	440	8	NH$_3$	260
PN440-16	440	16	NH$_3$	260
PN440-24	440	24	NH$_3$	260
PN440RE-8	440	8	NH$_3$	260
PN440RE-16	440	16	NH$_3$	260
PN440RE-24	440	24	NH$_3$	260

Microhardness (HV-1000IS, Shanghai Jvjing, Shanghai, China) was determined with a microhardness tester under an indentation load of 10 g for 15 s. According to GB/T 11354-2005 (determination of nitrided case depth and metallographic microstructure examination for steel iron parts) from the surface of the specimen to the Vickers hardness value of 50HV higher than the base of the vertical distance for the depth of the nitrided layer (termed the effective hardening layer). At least three microhardness indentations at each position were tested, and average values were used to ensure the accuracy of the microhardness profiles. To identify the phases of the compound layer, X-ray diffraction (XRD, Bruker, Billerica, MA, USA) with Cu-Kα radiation was carried out in a range of glancing degrees 20–100° at a voltage of 45 kV.

In order to evaluate the wear resistance of the nitrided layer, the HSR-2M friction and wear test machine was employed. In the wear test, the specimens were rubbed against a WC ball with a diameter of 5 mm under a load of 5 N at a speed of 200 r/min for 60 min and a rotation radius of 4 mm. The wear rate, η, was calculated according to the following equation:

$$\eta = \frac{\Delta m}{LN} \qquad (1)$$

where Δm is the mass difference before and after wear. L (m) is the total sliding distance. N is the normal contact load.

The potentiodynamic polarization tests were carried out to estimate the corrosion resistance of the specimens in a 3.5 wt.% NaCl solution, the reference electrode was Ag/AgCl, and a platinum column was used as the auxiliary electrode.

3. Results

3.1. Microstructure and Microhardness of Modified Layer

The cross-sectional microstructures of the PN440) and PN440RE specimens are depicted in Figure 1. Figure 1a–c show the microstructures of PN440-8, PN440-16, and PN440-24 with thicknesses of 10.2, 15.1, and 19.9 µm, respectively. Figure 1d–f show the microstructures of PN440RE-8, PN440RE-16, and PN440RE-24 with the thicknesses of 12.8, 17.9, and 21.6 µm, respectively. Compared to PN440, the nitrided layer thickened by 25.49%, 18.54%, and 8.54% for PN440RE, suggesting that the presence of La is likely to form a thicker nitrided layer within the same nitriding time.
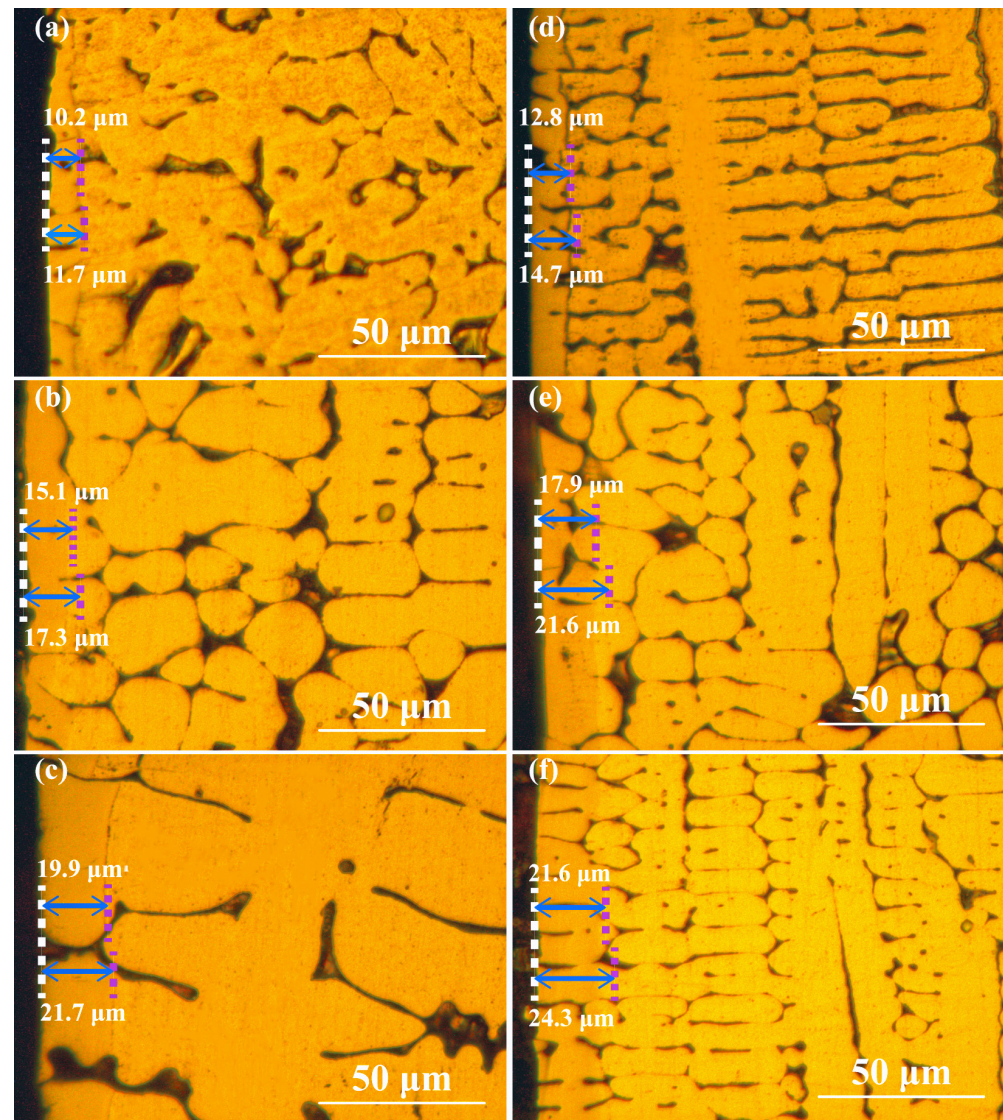

Figure 1. Microstructure of modified layer of CoCrCuFeNi HEA under different nitriding conditions: (**a**) PN440-8 h; (**b**) PN440-16 h; (**c**) PN440-24 h; (**d**) PN440RE-8 h; (**e**) PN440RE-16 h; (**f**) PN440RE-24 h.

Figure 2a,b show the hardness distribution from the surface to the core of CoCrCuFeNi HEA after nitriding at 440 °C. In Figure 2a, the hardness profiles of PN440-8, PN440-16, and PN440-24 are shown, with average surface hardness values of 1243.6, 1290, and 1307 HV0.01, respectively. The average hardnesses of the nitrided layer are 860, 1233, and 1096.8 HV0.01. In Figure 2b, the hardness profiles of PN440RE-8, PN440RE-16, and PN440RE-24 are presented with average surface hardness values of 1393, 1379, and 1466 HV0.01, respectively. The average hardness of the nitrided layer is 1132.3, 1170.6, and 1001 HV0.01. According to Figure 2, the hardness method (GB/T 11354-2005) can determine the effective hardening layer thickness of high-entropy alloys after nitriding. The effective hardening layer thicknesses of PN440 increase with time to 11.7 μm, 17.3 μm, and 21.7 μm, respectively, while for PN440RE, they increase to 14.7 μm, 21.6 μm, and 24.3 μm, respectively.
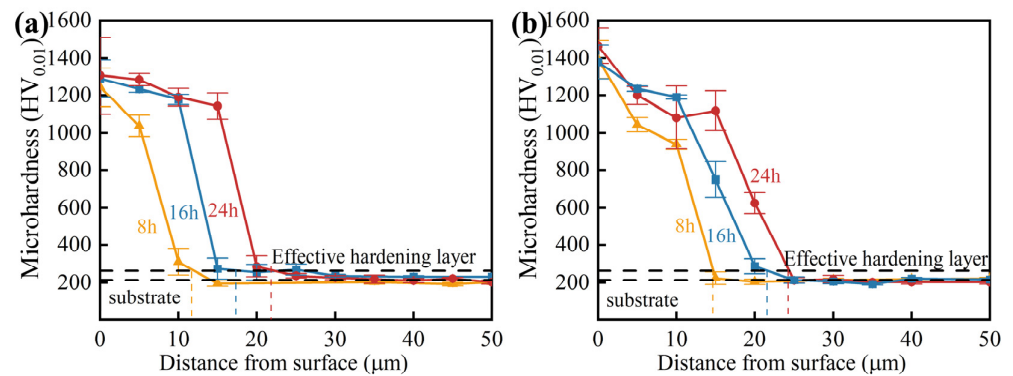

Figure 2. Microhardness profiles of modified layer cross-section under nitriding conditions for (**a**) PN440, (**b**) PN440RE.

Compared with the rapid decrease in hardness of PN440, La can adjust the organization of the nitrided layer of PN440RE after entering the specimen to make the hardness of PN440RE decrease more slowly. This suggests that the nitrided layer of PN440RE has a more evenly distributed nitrogen element [29,30].

3.2. Growth Kinetic of the Nitrided Layer

Figure 3a illustrates the relationship between treatment time and effective hardening layer thickness for PN440 and PN440RE treatments. The growth of the effective hardening layer in both treatments follows a parabolic law, increasing with treatment time. Notably, the effective hardening layer thickness is significantly more significant in the PN440RE treatment than in the PN440 treatment under equal treatment time. Based on hardness measurements (Section 3.1), the effective hardening layer of PN440RE-treated samples exhibited an increase of 25.64%, 24.85%, and 11.98% compared to PN440 at the corresponding treatment time. It is implied that adding La can accelerate the growth of the effective hardening layer.
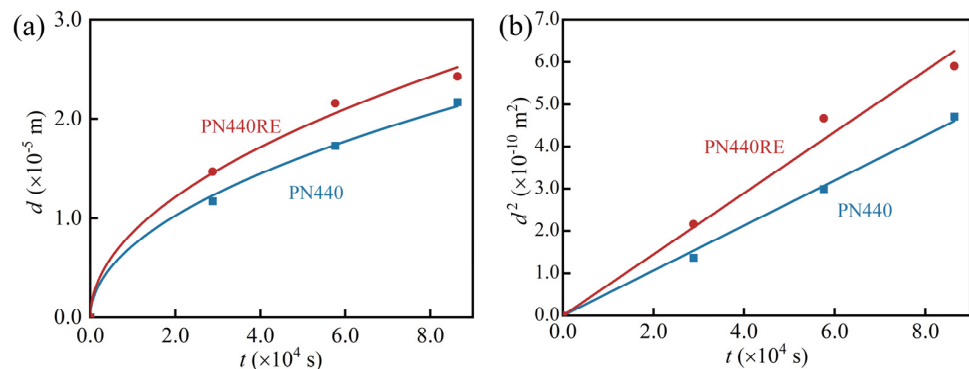

Figure 3. Layer growth kinetics of PN440 and PN440RE for different times: (**a**) effective hardening layer thickness vs. treating time, (**b**) the square of effective hardening layer thickness vs. treating time.

In order to compare more clearly the accelerating effect of the element La on the diffusion of N atoms, the diffusion coefficient is calculated by Equation (2) [31,32]:

$$d^2 = kt \tag{2}$$

where d is the effective hardening layer thickness, t is the treating time (s), and k is the growth rate constant. The linear relationship between the square of the effective hardening layer thickness and time can be observed, as depicted in Figure 3. Therefore, the growth rate constant k can be determined by the slope of each line for the different processes. Table 3 shows the growth rate constant k of HEA after treatment with PN440 and PN440RE. It is evident that the growth rate constant of PN440RE treatment surpasses that of PN440 treatment at the same temperature, implying that the addition of La into PN440RE can accelerate N atom diffusion and achieve higher diffusion efficiency (the diffusion efficiency of N atoms can attain the level observed in AISI 1045 steel during the plasma oxynitriding process at 783 k).

The mechanism by which La accelerate the diffusion of nitrogen atoms can be explained as follows. On the one hand, the La, once added to the treatment medium (NH_3), can act as a catalyst for a variety of chemical reactions in an nitriding atmosphere, by changing the reaction paths [31]. On the other hand, because La forms many anti-trapping regions [26] after entering the crystal, these anti-trapping regions repel nitrogen atoms and reduce the diffusion activation energy.

After incorporating La, plasma nitriding can be carried out at lower temperatures, thus reducing the nitriding time to achieve a similar effective hardening layer thickness. After 16 h of treatment with La, the increase in effective hardening layer thickness becomes limited (shown in Figure 1).

This phenomenon can be attributed to the limited activity of La atoms at lower temperatures [33]. Therefore, the introduction of La atoms into the lattice interior accelerates the diffusion of nitrogen atoms, which becomes the main factor for the increase in the thickness of the nitrided layer. The slower growth rate of the nitrided layer after being treated for 16 h may be attributed to the limited number of La atoms added during the PN440RE treatment in this study. These atoms (La atoms) were unable to diffuse to deeper locations.

Table 3. Growth rate constant in PN440 and PN440RE.

Process	Growth Rate Constant k (10^{-14} m^2/s)	
PN440	0.53	
PN440RE	0.72	
Plasma oxynitriding (AISI 1045)	0.821 (783k)	[34]
Plasma nitriding (AISI 1045)	0.28 (783k)	[34]

3.3. Phase Composition of the Modified Layer

Figure 4a,b show the X-ray diffraction patterns of PN440 and PN440RE at different treatment times. The nitrided layer of both PN440 and PN440RE is composed mainly of FCC, expanded FCC (FCC_N), Fe_4N, and CrN. The relative content of Fe_4N in the nitrided layer increases gradually with nitriding time. However, the diffraction intensity of the XRD diffraction peak of CrN (111) remains low and does not change significantly with the treatment time. Some scholars have demonstrated that CrN (expanded austenite will not decompose) is not formed below 450 °C [35–38]. Therefore, it can be assumed that trace amounts of CrN are formed on the surface of the specimen due to sputter deposition. The FCC_N is similar to the γ_N that occurs after nitriding austenitic stainless steels. The FCC can also be considered γ-Fe. This assumption has been shown to be the main component of the permeation layer after nitriding high- or medium-entropy alloys [39,40].
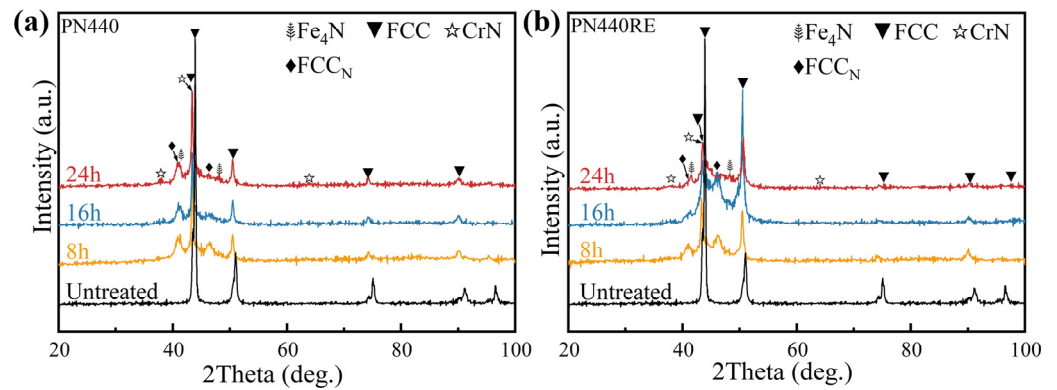
Figure 4. X-ray diffraction patterns of CoCrCuFeNi HEA without and with RE. (**a**) PN440, (**b**) PN440RE.

Table 4 presents the diffraction peak intensities and diffraction angles of FCC_N and Fe_4N. The FCC_N (200) of PN440 shifts towards a smaller angle with time, which is related to the lattice expansion caused by the interstitial solid solution of nitrogen with the increase in time [41]. The diffraction peaks of FCC_N (200) shift to a smaller angle after PN440RE treatment, in contrast to PN440. Additionally, the diffraction peaks of FCCN (200) shift to a larger angle with increasing treatment time. Furthermore, the diffraction peak angle of PN440RE (200) is larger than that of the FCC_N (200) of PN440, indicating that the interplanar distance of PN440RE is smaller. The cause of this phenomenon may be the acceleration of nitrogen atoms by La atoms, as explained in Section 3.2. In simpler terms, La reduces the diffusion activation energy of nitrogen atoms, which results in the easier migration of nitrogen atoms to the next interstitial position, resulting in fewer nitrogen atoms inside the FCC lattice (due to the lower concentration of nitrogen atoms capable of triggering their diffusion). The X-ray diffraction peak angle of Fe_4N after PN440 and PN440RE treatments remained almost unchanged, only the diffraction intensity changed.

Table 4. List of the phases identified in X-ray diffraction patterns with their crystallographic data.

	2θ (°)	Intensity (a.u.)	Phase	Plane (*hkl*)
untreated	43.90	828.30	FCC	111
	51.02	156.20	FCC	200
	75.08	76.30	FCC	220
PN440-8	40.86	63.80	FCC_N	111
	46.46	46.60	FCC_N	200
	41.26	67.70	Fe_4N	111
	48.06	27.00	Fe_4N	200
PN440-16	40.90	40.50	FCC_N	111
	46.36	27.50	FCC_N	200
	41.26	44.60	Fe_4N	111
	48.06	12.80	Fe_4N	200
PN440-24	40.94	58.20	FCC_N	111
	46.28	36.50	FCC_N	200
	41.40	49.70	Fe_4N	111
	48.12	36.00	Fe_4N	200
PN440RE-8	40.86	41.70	FCC_N	111
	46.04	63.10	FCC_N	200
	41.32	31.40	Fe_4N	111
	48.22	26.90	Fe_4N	200
PN440RE-16	41.02	32.40	FCC_N	111
	46.18	120.10	FCC_N	200
	41.38	31.70	Fe_4N	111
	48.12	54.20	Fe_4N	200

Table 4. *Cont.*

	2θ (°)	Intensity (a.u.)	Phase	Plane (*hkl*)
PN440RE-24	41.04	25.60	FCC$_N$	111
	46.70	35.80	FCC$_N$	200
	41.52	32.20	Fe$_4$N	111
	48.14	30.30	Fe4N	200

3.4. Corrosion Properties of the Nitrided Layer

The polarization curve data of PN440 in Figure 5a were used for fitting, and the fitting results are shown in Table 5. From the data in Table 5, it can be seen that the passivation zone of the corrosion resistance curve of PN440 becomes wider, the corrosion current density and corrosion rate decrease, and the corrosion potential increases with the extension of the treatment time. Among the samples, PN440-24 has the best corrosion resistance. Experimentally, it has been proven that under the PN440 process, the longer the treatment time, the better the corrosion resistance. The change in corrosion resistance can be related to the concentration of interstitial nitrogen atoms in FCC$_N$ [36,42]. When an austenitic stainless steel containing interstitial nitrogen is subjected to pitting, interstitial nitrogen atoms are released. The released nitrogen atoms can react with H$^+$ to form NH$_4^+$ [43]. Table 4 shows the change in the angle of the FCC$_N$ (200) diffraction peak of PN440, and the rule of change is that the angle of the diffraction peak is shifted to a small angle with the increase in the treatment time. It shows that the interplanar distance of FCC$_N$ (200) becomes larger, which means that the concentration of interstitial nitrogen atoms inside the FCC$_N$ lattice increases with treatment time. Therefore, the corrosion resistance of PN440 becomes stronger as the treatment time increases.
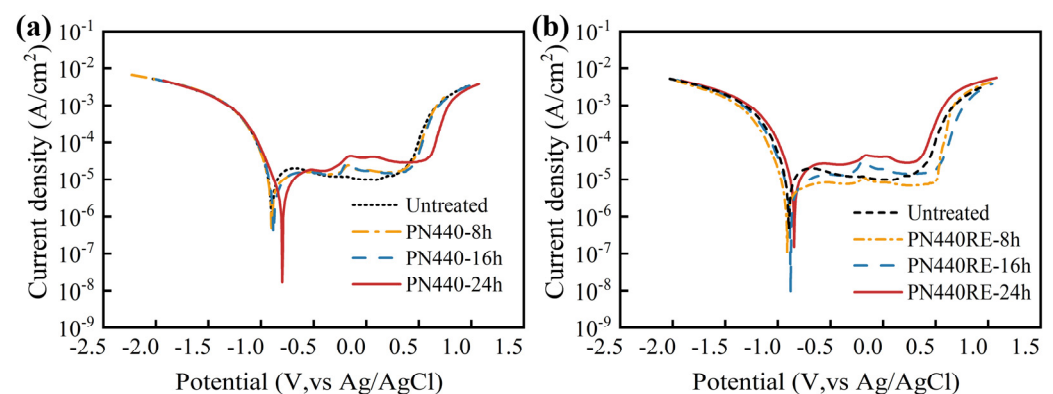

Figure 5. Corrosion resistance curve of modified layer of HEA after plasma nitriding at different times. (**a**) PN440 (**b**) PN440RE.

Table 5. Fitting data of the polarization curve of the modified layer of PN440.

	Untreated	8 h	16 h	24 h
Corrosion rate ($\times 10^{-2}$ mm/a)	6.89	6.05	4.92	3.45
Io ($\times 10^{-6}$ A/cm^2)	5.92	5.20	4.24	2.96
Eo/V	−0.88	−0.89	−0.87	−0.79
Passivation zone width/V	1.17	1.27	1.30	1.36

By analyzing the polarization curve data in Figure 5b and the fitting results in Table 6, it can be seen that the corrosion rate and corrosion current density of PN440RE-8 to PN440RE-16 decrease significantly while the passivation zone expands. On the contrary, for PN440RE-16 to PN440RE-24, the corrosion rate and current density increase slightly while the passivation zone shrinks significantly. Table 4 shows that the diffraction peak angle of the FCC$_N$ of PN440RE-24 is smaller than that of PN440RE-16, indicating that the

FCC_N of PN440RE-24 has a smaller interplanar distance. This also means that there are fewer interstitial nitrogen atoms in the FCC_N after treatment of PN440RE-24, resulting in a decrease in the corrosion resistance of PN440RE-24.

Table 6. Fitting data of the polarization curve of the modified layer of PN440RE.

	Untreated	**8 h**	**16 h**	**24 h**
Corrosion rate ($\times 10^{-2}$ mm/a)	6.89	2.83	2.50	5.21
Io ($\times 10^{-6}$ A/cm^2)	5.92	2.43	2.13	4.48
Eo/V	−0.88	−0.91	−0.87	−0.84
Passivation zone width/V	1.17	1.36	1.39	1.16

3.5. Friction Performance Analysis

Figure 6a displays the surface friction coefficient curves of the CoCrCuFeNi high-entropy alloy after nitriding. Figure 6b shows the friction coefficient curves of the CoCrCuFeNi high-entropy alloy after nitriding. By combining this with Figure 7a, it is possible to obtain the stable friction coefficients at 8, 16, and 24 h of nitriding, which are 0.71, 0.56, and 0.62, respectively. The stabilized friction coefficients after nitriding for 8, 16, and 24 h are 0.79, 0.59, and 0.48, respectively, as shown in Figure 7b.
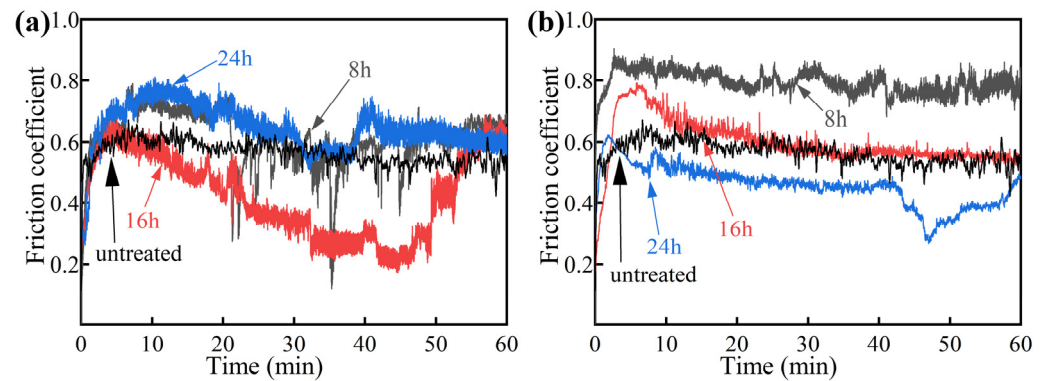

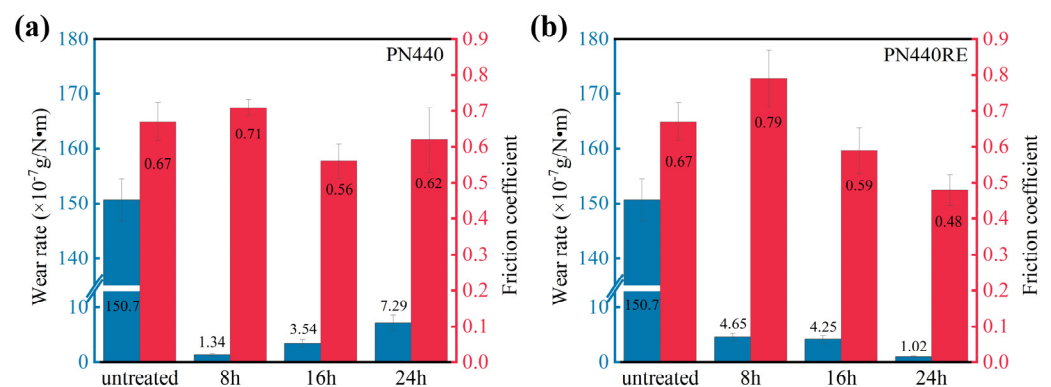**Figure 6.** Friction coefficient curve of CoCrCuFeNi high-entropy alloy after nitriding at 440 °C. (**a**) PN440, (**b**) PN440RE.

Figure 7. Wear rates and friction coefficient of CoCrCuFeNi high-entropy alloy treated by NH$_3$ at 440 °C. (**a**) PN440; (**b**) PN440RE.

The friction coefficient curves of the PN440-treated specimens exhibited more fluctuations than those of PN440RE, as shown in Figure 6a. Additionally, a stick-slip behavior characterized by a sudden drop in the curve was observed for the PN440-treated specimens. This phenomenon can be explained by the "oxidation-scrape-reoxidation" theory [44]. According to this theory, wear debris alternately undergo oxidation, compaction and

delamination processes on the friction surface [45] during the wear process, leading to oscillation of the friction coefficient.

The wear rates of the PN440 treatment after 8, 16, and 24 h are 1.34×10^{-7} g/N·m, 3.45×10^{-7} g/N·m, and 7.29×10^{-7} g/N·m, respectively, as shown in Figure 7a. Zhang et al. [46] also observed this phenomenon. The change in wear rate is attributed to oxidative wear at lower sliding velocities, which destroys the oxide film during the wear process.

The EDS analysis in this study indicates that oxidative wear occurred during the wear process. Figure 8a,c shows traces of adhesive wear [47,48] and fragmented oxide particles on the wear track surface, indicating a high degree of oxide film breakage. These changes affect the nitrided wear rate without the addition of La.
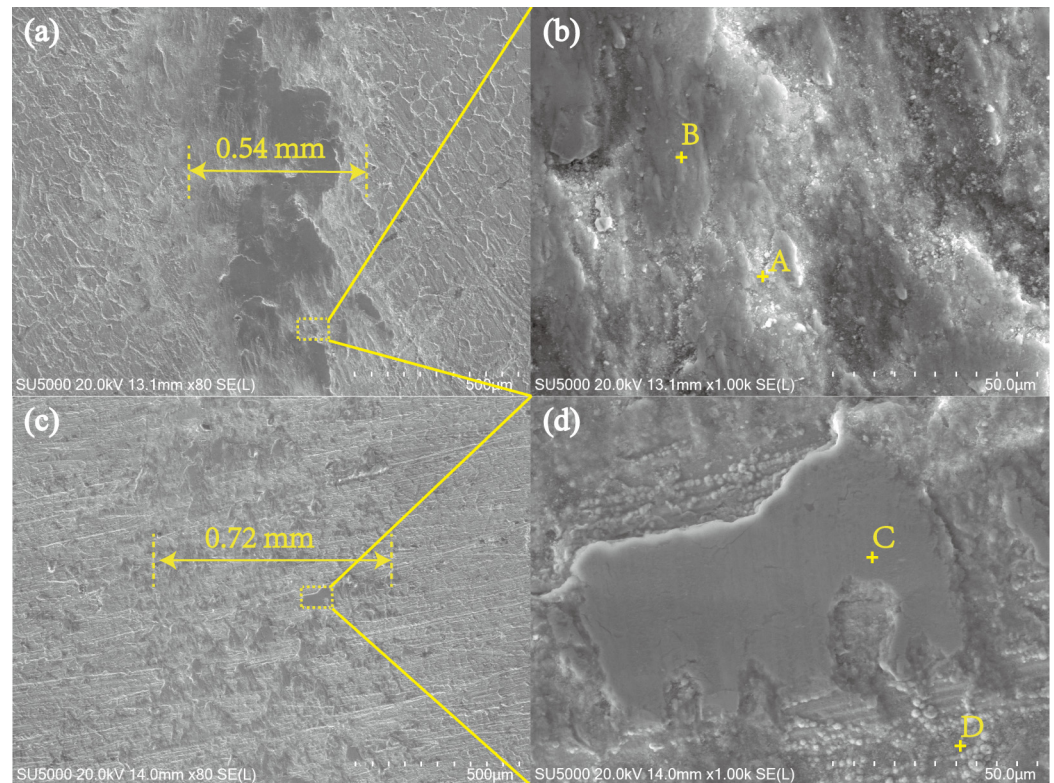

Figure 8. Wear morphologies of CoCrCuFeNi high-entropy alloy after wear test. (**a**) PN440-24; (**c**) PN440RE-24; Enlarged Image of a localized wear track, (**b**) PN440-24; (**d**) PN440RE-24.

Figure 7b displays the wear rates of PN440RE after 8, 16, and 24 h, which were 4.65×10^{-7} g/N·m, 4.25×10^{-7} g/N·m, and 1.02×10^{-7} g/N·m, respectively. The wear rate decreases with nitriding time after adding La. This is likely due to the increase in relative Fe_4N content with the longer nitriding time and the fact that the oxide film is not severely damaged during wear, as shown in Figure 8a (with many fewer adhesive wear traces compared to PN440-24).

Figure 8 shows the surface wear morphology of the CoCrCuFeNi high-entropy alloy after two nitriding processes. In Figure 8a, friction abrasion marks are visible after the wear test of PN440-24. The width of the abrasion marks is 0.54 mm, and a higher number of traces of adhesive wear (dark-colored flakes) can be observed. Therefore, the wear mechanism of PN440-24 is more severe adhesive wear. Figure 8c shows the wear marks of PN440RE-24 after the wear test. The width of the wear marks is 0.72 mm. Compared to PN440, there are fewer traces of adhesive wear on the wear marks of PN440RE. Therefore, the wear mechanism of PN440RE-24 is slight adhesive wear.

Table 7 shows the chemical compositions of points A, B, C, and D in Figure 8b,d. Each point A, B, C, and D exhibits a higher concentration of elemental oxygen, indicating that the wear mechanism of PN440-24 and PN440RE-24 involves both adhesive and oxidative wear.

Table 7. Semi-quantitative EDS analysis for the signed regions (wt.%) shown in Figure 8b,d.

Elements	A	B	C	D
N	0	0	0	0.91
O	25.26	25.19	30.02	15.25
Cr	2.68	2.75	23.64	14.34
Fe	67.35	67.26	64.18	36.70
Co	1.31	1.33	0.93	13.53
Ni	1.14	1.13	0.61	10.57
Cu	2.25	2.34	1.02	7.97
W	0	0	0.61	0.71

4. Conclusions

The study successfully employed the method of the addition of La to the plasma nitriding process to increase the growth rate of the effective hardening layer and overcome the sluggish diffusion effect of high-entropy alloys. This resulted in a better quality nitrided layer in a shorter nitriding time. From the experimental data, it is possible to draw the following conclusions:

1. The thickness of the nitrided layer of PN440RE increased by 25.49%, 18.54%, and 8.54% compared to PN440, suggesting that La may contribute to a thicker nitrided layer for the same nitriding time. The hardness curve indicates a more homogeneous distribution of nitrogen atoms in the nitrided layer of PN440RE.
2. The effective hardening layer versus time curve shows that the growth of the effective hardening layer of PN440 and PN440RE follows a parabolic law. This means that the plasma nitriding of CoCrCuFeNi high-entropy alloys is diffusion-controlled, and the effective hardening layer thickness growth is limited after 16 h of nitriding treatment with La. The results indicate that the addition of La can produce a higher quality effective hardening layer in a shorter time.
3. The phase composition of the nitrided layer is affected by the nitriding time. Specifically, as the nitriding time increases, the diffraction peak angle of FCC_N changes differently in PN440 and PN440RE. After the PN440 treatment, the diffraction peak angle of FCC_N shifts toward a smaller angle, while the opposite is true for PN440RE.
4. Corrosion resistance is determined by the concentration of interstitial nitrogen atoms in the FCC_N lattice of the nitrided layer. The angle of the diffraction peak of FCC_N can determine the nitrogen concentration. A smaller diffraction peak angle indicates a larger interplanar distance, higher nitrogen concentration, and better corrosion resistance.
5. Both PN440-24 and PN440RE-24 experience oxidative wear accompanied by adhesive wear. However, due to the higher level of adhesive wear in PN440-24, the wear rate of PN440RE-24 is 86.0% lower than that of PN440-24.

Author Contributions: Conceptualization, Y.W. (Yifan Wang) and Y.Y.; methodology, Y.W. (Yifan Wang) and Y.Y.; formal analysis, Y.Y.; investigation, Y.W. (Yifan Wang), W.S., Y.W. (Yan Wang), and S.X.; resources, Y.Y. and M.Y.; data curation, Y.Y., F.G., C.W., W.C. and Y.Z.; writing—review and editing, Y.W. (Yifan Wang) and Y.Y.; visualization, Y.W. (Yifan Wang); supervision, M.Y.; project administration, Y.Y. and M.Y.; funding acquisition, Y.Y and M.Y. All authors have read and agreed to the published version of the manuscript.

Institutional Review Board Statement: Not applicable.

Informed Consent Statement: Not applicable.

Data Availability Statement: Data are contained within the article.

Conflicts of Interest: The authors declare that they have no conflict of interest.

References

1. Yeh, J.W.; Chen, S.-K.; Lin, S.-J.; Gan, J.-Y.; Chin, T.S.; Shun, T.-T.; Tsau, C.H.; Chang, S.Y. Nanostructured High-Entropy Alloys with Multiple Principal Elements: Novel Alloy Design Concepts and Outcomes. *Adv. Eng. Mater.* **2004**, *6*, 299–303. [CrossRef]
2. Kumar, D.; Seetharam, R.; Ponappa, K. A Review on Microstructures, Mechanical Properties and Processing of High Entropy Alloys Reinforced Composite Materials. *J. Alloys Compd.* **2024**, *972*, 172732. [CrossRef]
3. Wan, W.; Liang, K.; Zhu, P.; He, P.; Zhang, S. Recent Advances in the Synthesis and Fabrication Methods of High-Entropy Alloy Nanoparticles. *J. Mater. Sci. Technol.* **2024**, *178*, 226–246. [CrossRef]
4. Yeh, J.W. Alloy Design Strategies and Future Trends in High-Entropy Alloys. *JOM* **2013**, *65*, 1759–1771. [CrossRef]
5. Zhang, Y.; Qiao, J.W.; Liaw, P.K. A Brief Review of High Entropy Alloys and Serration Behavior and Flow Units. *J. Iron Steel Res. Int.* **2016**, *23*, 2–6. [CrossRef]
6. Liu, L.Y.; Zhang, Y.; Han, J.H.; Wang, X.Y.; Jiang, W.Q.; Liu, C.T.; Zhang, Z.W.; Liaw, P.K. Nanoprecipitate-Strengthened High-Entropy Alloys. *Adv. Sci.* **2021**, *8*, 2100870. [CrossRef]
7. Chaudhary, V.; Soni, V.; Gwalani, B.; Ramanujan, R.V.; Banerjee, R. Influence of Non-Magnetic Cu on Enhancing the Low Temperature Magnetic Properties and Curie Temperature of Feconicrcu(X) High Entropy Alloys. *Scr. Mater.* **2020**, *182*, 99–103. [CrossRef]
8. Yu, H.-Y.; Fang, W.; Chang, R.-B.; Ji, P.-G.; Wang, Q.-Z. Modifying Element Diffusion Pathway by Transition Layer Structure in High-Entropy Alloy Particle Reinforced Cu Matrix Composites. *Trans. Nonferrous Met. Soc. China* **2019**, *29*, 2331–2339. [CrossRef]
9. Hemphill, M.A.; Yuan, T.; Wang, G.Y.; Yeh, J.W.; Tsai, C.W.; Chuang, A.; Liaw, P.K. Fatigue Behavior of Al0.5cocrcufeni High Entropy Alloys. *Acta Mater.* **2012**, *60*, 5723–5734. [CrossRef]
10. Huang, G.Q.; Li, B.; Chen, Y.N.; Xuan, F.Z. Nanotwining Induced by Tensile Fatigue and Dynamic Impact of Laser Powder B E D Fusion Additively Manufactured Cocrfeni High-Entropy Alloy. *J. Mater. Sci. Technol.* **2024**, *183*, 241–257. [CrossRef]
11. Feng, R.; Feng, B.J.; Gao, M.C.; Zhang, C.; Neuefeind, J.C.; Poplawsky, J.D.; Ren, Y.; An, K.; Widom, M.; Liaw, P.K. Superior High-Temperature Strength in a Supersaturated Refractory High-Entropy Alloy. *Adv. Mater.* **2021**, *33*, 2102401. [CrossRef] [PubMed]
12. Chang, Y.J.; Yeh, A.C. The Evolution of Microstructures and High Temperature Properties of $Al_XCo_{1.5}Crfeni_{1.5}Ti_Y$ High Entropy Alloys. *J. Alloys Compd.* **2015**, *653*, 379–385. [CrossRef]
13. Zhang, H.T.; Wang, C.L.; Miao, J.W.; Shi, S.Y.; Li, T.J.; Yan, H.W.; Zhang, Y.A.; Lu, Y.P. Effect of Microstructure Evolution on Wear Resistance of Equal Molar Cocrfeni High-Entropy Alloy. *Rare Metals* **2023**, *42*, 3797–3805. [CrossRef]
14. Wang, K.; Huang, J.; Chen, H.; Wang, Y.; Yan, W.; Yuan, X.; Song, S.; Zhang, J.; Sun, X. Recent Progress in High Entropy Alloys for Electrocatalysts. *Electrochem. Energy Rev.* **2022**, *5*, 17. [CrossRef]
15. Pickering, E.J.; Jones, N.G. High-Entropy Alloys: A Critical Assessment of Their Founding Principles and Future Prospects. *Int. Mater. Rev.* **2016**, *61*, 183–202. [CrossRef]
16. Meng, F.; Baker, I. Nitriding of a High Entropy Fenimnalcr Alloy. *J. Alloys Compd.* **2015**, *645*, 376–381. [CrossRef]
17. Chen, R.; Cai, Z.; Pu, J.; Lu, Z.; Chen, S.; Zheng, S.; Zeng, C. Effects of Nitriding on the Microstructure and Properties of Valticrmo High-Entropy Alloy Coatings by Sputtering Technique. *J. Alloys Compd.* **2020**, *827*, 153836. [CrossRef]
18. Tang, W.-Y.; Chuang, M.-H.; Lin, S.-J.; Yeh, J.-W. Microstructures and Mechanical Performance of Plasma-Nitrided Al0.3crfe1.5mnni0.5 High-Entropy Alloys. *Metall. Mater. Trans. A* **2012**, *43*, 2390–2400. [CrossRef]
19. Tang, W.-Y.; Chuang, M.-H.; Chen, H.-Y.; Yeh, J.-W. Microstructure and Mechanical Performance of New Al0.5crfe1.5mnni0.5 High-Entropy Alloys Improved by Plasma Nitriding. *Surf. Coat. Technol.* **2010**, *204*, 3118–3124. [CrossRef]
20. Tang, W.-Y.; Yeh, J.-W. Effect of Aluminum Content on Plasma-Nitrided Alxcocrcufeni High-Entropy Alloys. *Metall. Mater. Trans. A* **2009**, *40*, 1479–1486. [CrossRef]
21. Lan, L.W.; Wang, X.J.; Guo, R.P.; Yang, H.J.; Qiao, J.W. Effect of Environments and Normal Loads on Tribological Properties of Nitrided Ni45(Fecocr)40(Alti)15 High-Entropy Alloys. *J. Mater. Sci. Technol.* **2020**, *42*, 85–96. [CrossRef]
22. Karimoto, T.; Nishimoto, A. Plasma-Nitriding Properties of Cocrfemnni High-Entropy Alloys Produced by Spark Plasma Sintering. *Metals* **2020**, *10*, 761. [CrossRef]
23. Nishimoto, A.; Fukube, T.; Maruyama, T. Microstructural, Mechanical, and Corrosion Properties of Plasma-Nitrided Cocrfemnni High-Entropy Alloys. *Surf. Coat. Technol.* **2019**, *376*, 52–58. [CrossRef]
24. Peng, J.; Dong, H.; Bell, T.; Chen, F.; Mo, Z.; Wang, C.; Peng, Q. Effect of Rare Earth Elements on Plasma Nitriding of 38crmoai Steel. *Surf. Eng.* **1996**, *12*, 147–151. [CrossRef]
25. Bell, T.; Sun, Y.; Lui, Z.; Yan, M. Rare-Earth Surface Engineering. *Heat Treat. Met.* **2000**, *27*, 1–8.
26. You, Y.; Yan, J.; Yan, M. Atomistic Diffusion Mechanism of Rare Earth Carburizing/Nitriding on Iron-Based Alloy. *Appl. Surf. Sci.* **2019**, *484*, 710–715. [CrossRef]
27. Liu, D.J.; You, Y.; Yan, M.F.; Chen, H.T.; Li, R.; Hong, L.; Han, T.J. Acceleration of Plasma Nitriding at 550 °C with Rare Earth on the Surface of 38crmoal Steel. *Coatings* **2021**, *11*, 1122. [CrossRef]
28. Tang, L.N.; Yan, M.F. Microstructure and Corrosion Resistance of Quenched Aisi 4140 Steel Plasma Nitrided and Nitrocarburised with and without Rare Earths. *Mater. Sci. Technol.* **2013**, *29*, 610–615. [CrossRef]

29. You, Y.; Li, R.; Yan, M.; Yan, J.; Chen, H.; Wang, C.; Liu, D.; Hong, L.; Han, T. Low-Temperature Plasma Nitriding of 3cr13 Steel Accelerated by Rare-Earth Block. *Coatings* **2021**, *11*, 1050. [CrossRef]

30. Xie, W.; Chen, Y.; Chen, D.; Yang, Y.; Zhang, C.; Cui, G.; Wang, Y. Low-Pressure Gas Nitriding of Aisi 304 Austenitic Stainless Steel: Reducing the Precipitation of Chromium Nitrides. *Mater. Res. Express* **2020**, *7*, 066406. [CrossRef]

31. Liu, R.L.; Yan, M.F.; Wu, Y.Q.; Zhao, C.Z. Microstructure and Properties of 17-4ph Steel Plasma Nitrocarburized with a Carrier Gas Containing Rare Earth Elements. *Mater. Charact.* **2010**, *61*, 19–24. [CrossRef]

32. Chen, F.-S.; Wang, K.-L. The Kinetics and Mechanism of Multi-Component Diffusion on Aisi 1045 Steel. *Surf. Coat. Technol.* **1999**, *115*, 239–248. [CrossRef]

33. Liu, R.L.; Qiao, Y.J.; Yan, M.F.; Fu, Y.D. Layer Growth Kinetics and Wear Resistance of Martensitic Precipitation Hardening Stainless Steel Plasma Nitrocarburized at 460 °C with Rare Earth Addition. *Met. Mater. Int.* **2013**, *19*, 1151–1157. [CrossRef]

34. Liu, H.; Li, J.; Chai, Y.; Wei, W.; Hu, J. Kinetics and Enhancement Mechanism of Plasma Oxynitriding for Aisi 1045 Steel. *Surf. Coat. Technol.* **2016**, *302*, 22–26. [CrossRef]

35. Li, C.X.; Bell, T. Corrosion Properties of Active Screen Plasma Nitrided 316 Austenitic Stainless Steel. *Corros. Sci.* **2004**, *46*, 1527–1547. [CrossRef]

36. Fossati, A.; Borgioli, F.; Galvanetto, E.; Bacci, T. Corrosion Resistance Properties of Glow-Discharge Nitrided Aisi 316l Austenitic Stainless Steel in Nacl Solutions. *Corros. Sci.* **2006**, *48*, 1513–1527. [CrossRef]

37. Borgioli, F.; Galvanetto, E.; Bacci, T. Low Temperature Nitriding of Aisi 300 and 200 Series Austenitic Stainless Steels. *Vacuum* **2016**, *127*, 51–60. [CrossRef]

38. Xie, Y.L.; Miyamoto, G.; Furuhara, T. Nanosized Cr-N Clustering in Expanded Austenite Layer of Low Temperature Plasma-Nitrided Fe-35ni-10cr Alloy. *Scr. Mater.* **2022**, *213*, 114637. [CrossRef]

39. Tao, X.; Yang, Y.; Qi, J.; Cai, B.; Rainforth, W.M.; Li, X.; Dong, H. An Investigation on Nitrogen Uptake and Microstructure of Equimolar Quaternary Feconicr High Entropy Alloy after Active-Screen Plasma Nitriding. *Mater. Charact.* **2024**, *208*, 113593. [CrossRef]

40. Tao, X.; Yang, Y.P.; Qi, J.H.; Cai, B.; Rainforth, W.M.; Li, X.Y.; Dong, H.S. Active Screen Plasma Nitriding of a Si-Alloyed Fecrni Medium Entropy Alloy: High Interstitial Absorption and an Anomalous Si-Induced Decomposition Mechanism in N-Expanded Austenite. *Appl. Surf. Sci.* **2023**, *624*, 157137. [CrossRef]

41. Qin, X.; Guo, X.; Lu, J.; Chen, L.; Qin, J.; Lu, W. Erosion-Wear and Intergranular Corrosion Resistance Properties of Aisi 304l Austenitic Stainless Steel after Low-Temperature Plasma Nitriding. *J. Alloys Compd.* **2017**, *698*, 1094–1101. [CrossRef]

42. Baba, H.; Kodama, T.; Katada, Y. Role of Nitrogen on the Corrosion Behavior of Austenitic Stainless Steels. *Corros. Sci.* **2002**, *44*, 2393–2407. [CrossRef]

43. Dong, H. S-Phase Surface Engineering of Fe-Cr, Co-Cr and Ni-Cr Alloys. *Int. Mater. Rev.* **2010**, *55*, 65–98. [CrossRef]

44. Stott, F.H. The Role of Oxidation in the Wear of Alloys. *Tribol. Int.* **1998**, *31*, 61–71. [CrossRef]

45. Cui, X.H.; Wang, S.Q.; Wang, F.; Chen, K.M. Research on Oxidation Wear Mechanism of the Cast Steels. *Wear* **2008**, *265*, 468–476. [CrossRef]

46. Zhang, C.S.; Yan, M.F.; Sun, Z.; Wang, Y.X.; You, Y.; Bai, B.; Chen, L.; Long, Z.; Li, R.W. Optimizing the Mechanical Properties of M50nil Steel by Plasma Nitrocarburizing. *Appl. Surf. Sci.* **2014**, *315*, 28–35. [CrossRef]

47. Liu, L.; Shen, H.H.; Liu, X.Z.; Guo, Q.; Meng, T.X.; Wang, Z.X.; Yang, H.J.; Liu, X.P. Wear Resistance of Tin(Ti2N)/Ti Composite Layer Formed on C17200 Alloy by Plasma Surface Ti-Alloying and Nitriding. *Appl. Surf. Sci.* **2016**, *388*, 103–108. [CrossRef]

48. Naeem, M.; Díaz-Guillén, J.C.; Khalid, A.; Guzman-Flores, I.; Muñoz-Arroyo, R.; Iqbal, J.; Sousa, R.R.M. Improved Wear Resistance of Aisi-1045 Steel by Hybrid Treatment of Plasma Nitriding and Post-Oxidation. *Tribol. Int.* **2022**, *175*, 107869. [CrossRef]